Available online at www.sciencedirect.com

SciVerse ScienceDirect

Acta Materialia 61 (2013) 2571–2582

Acta MATERIALIA

www.elsevier.com/locate/actamat

Three-dimensional quantitative in situ study of crack initiation and propagation in AA6061 aluminum alloy sheets via synchrotron laminography and finite-element simulations

Yang Shen [a,b,*], Thilo F. Morgeneyer [b], Jérôme Garnier [a], Lucien Allais [a], Lukas Helfen [c,d], Jérôme Crépin [b]

[a] CEA, DEN, DMN, SRMA, F-91191 Gif-sur-yvette Cedex, France
[b] Mines ParisTech, Centre des Matériaux, CNRS UMR 7633, BP87 91003 Evry Cedex, France
[c] ANKA/Institute for Photon Science and Synchrotron Radiation, Karlsruhe Institute of Technology (KIT), D-76131 Karlsruhe, Germany
[d] European Synchrotron Radiation Facility (ESRF), BP 220, F-38043 Grenoble Cedex, France

Received 2 November 2012; received in revised form 20 January 2013; accepted 20 January 2013
Available online 14 February 2013

Abstract

Ductile crack initiation and propagation in AA6061 aluminum alloy for a fatigue precrack have been studied in situ via synchrotron radiation computed laminography, a technique specifically developed for three-dimensional imaging of laterally extended sheet specimens with micrometer resolution. The influence of the microstructure, i.e. due to the presence of coarse Mg_2Si precipitates and iron-rich intermetallics, on the void nucleation process is investigated. Coarse Mg_2Si precipitates are found to play a preponderant role in the void nucleation and ductile fracture process. Void growth and void coalescence are then observed and quantified by three-dimensional image analysis during crack initiation and propagation. Parameters for a Gurson–Tvergaard–Needleman micromechanical damage model are identified experimentally and validated by finite-element simulations.

Keywords: Crack propagation; AA6061 aluminum alloy; In situ laminography; Micromechanical modeling; Ductile fracture

1. Introduction

The improvement of the damage resistance is a critical criterion for the selection and use of light alloys. The tolerance for the presence of cracks is one of the crucial material properties for engineering components. The assessment of the complete crack initiation and propagation process may help to improve the material microstructure and to predict the lifetime of components and to delay their final fracture [1,2].

AA6061 aluminum alloy is often used for its light weight, good mechanical properties and good resistance to intergranular corrosion [3]. However, its relatively low resistance to crack propagation limits its utility, for instance in pressurized structures. Coarse intergranular precipitates in the alloy are responsible for the damage since they progressively become cavities during the loading processes and define a preferred path of crack propagation [4]. Two types of precipitates at the micrometer scale are present in this material: coarse Mg_2Si and iron-rich intermetallics [5,6]. Several authors have revealed the role played by the iron-rich intermetallics in the damage sequence of AA6061 alloys. For example, Blind et al. [7] have shown that the more intermetallics are present in the microstructure, the more reduced is the toughness of the alloy. Few authors have differentiated the role played by the two types of coarse precipitates in the damage mechanism. In fact, most authors showed that damage from coarse Mg_2Si precipitates is often negligible compared to the iron-rich intermetallics for two reasons [6,8–10]. First

* Corresponding author at: CEA, DEN, DMN, SRMA, F-91191 Gif-sur-yvette Cedex, France. Tel.: +33 169082279; fax: +33 169087167.
E-mail address: yang.shen@mines-nancy.org (Y. Shen).

1359-6454/$36.00 © 2013 Acta Materialia Inc. Published by Elsevier Ltd. All rights reserved.
http://dx.doi.org/10.1016/j.actamat.2013.01.035

of all, the fraction of coarse Mg_2Si precipitates is low compared to the intermetallics in the alloys of these studies. Secondly, the distinction between coarse Mg_2Si precipitates and cavities is difficult because of their low imaging contrast, e.g. dark gray for Mg_2Si and black for cavities in images obtained by scanning electron microscopy (SEM). In this work, the roles of these two types of precipitates during damage propagation in the bulk will be assessed via synchrotron-based three-dimensional (3-D) imaging of regions of interest inside the alloy sheet.

In order to investigate the damage sequence during the crack initiation and propagation, two-dimensional (2-D) observations have often been used for toughness tests/investigations [11]. However, this implies that on the one hand only surfaces can be observed in situ [6] where the levels of stress triaxiality are low and the fracture mechanisms are considerably different from the material bulk [12,13]. On the other hand, 2-D section observations in the inner of materials are destructive, thus in situ investigations become impossible. Synchrotron radiation computed tomography (SRCT) can be used to determine in situ damage evolution in bulk materials, with the cross-section of specimens in the order of 1 mm for μm-scale resolution. With this method, the authors [14,15] quantified the 3-D damage evolution in aluminum alloys during tensile tests. Despite the great success of SRCT for cylindrical specimens, it is difficult to image the local microstructure when the sample size significantly exceeds the field of view (~1.5 mm) of the detector, such as flat, laterally extended specimens since the strongly varying X-ray transmission during a scan is prone to generate imaging artifacts. As a consequence, laterally extended precracked specimens couldn't be used to assess the crack initiation and propagation by SRCT. Toda et al. [16] successfully analyzed crack initiation and propagation behaviors in a small I-shaped specimen extracted from a precracked single-edge notched specimen. However, the boundary condition of the small precracked specimen with a section of $1 \times 1.6\ mm^2$ is far from standard tests as the plastic zone at the crack tip is possibly larger than the specimen thickness.

To overcome these limits, synchrotron radiation computed laminography (SRCL) [17] is applied, which allows high-resolution non-destructive 3-D imaging in flat but laterally extended specimens. This method provides a unique means to observe and analyze damage evolution in three dimensions during the crack initiation and propagation in material specimens with intact sheet or panel geometries [18,19]. A qualitative description of the damage evolution has already been given for a ductile AA2139-T3 alloy [20]. The possibility to measure displacement and strain fields in three dimensions in situ has been demonstrated and possible limitations concerning the measurement accuracy estimated [21].

Traditionally, the damage evolution has been described by local approach modeling. The simplest one is the Rice–Tracey uncoupled damage model [22] based on analytical approaches for the growth of spherical voids in a perfectly plastic infinite matrix. A more complete model incorporating void initiation, growth and coalescence processes is the Gurson–Tvergaard–Needleman (GTN) coupled constitutive model [23,24] based on micromechanics. Generally, there is no unique method to determine the model parameters. Some of them depend on stress triaxiality and thus are calibrated by multiscale simulation [25,26] and others are obtained by fitting the numerical calculations with experimental results.

In the present study, ductile damage evolution during crack initiation and propagation is investigated quantitatively in a 1 mm thick fatigue-precracked specimen of an AA6061-T6 alloy via SRCL. These experimental results are then used for determination of parameters of the GTN damage model. This is to our knowledge the first model parameter calibration via observation of crack propagation in the bulk, which serves not only as initial model input data, but also for the final failure parameters. The model is then validated by comparing simulated and experimentally obtained load–displacement curves.

2. Experimental

2.1. Materials

A forged AA6061 alloy was used in this study whose chemical composition is given in Table 1. The material used was in the T6 temper (solution-heat-treated at 530 °C for 3 h, water-quenched and aged at 175 °C for 12 h). The heat treatment was defined to obtain the maximum yield stress. The majority of coarse Mg_2Si precipitates and iron-rich intermetallics are intergranular with a preferential alignment along the forging direction [5]. The volume fraction of coarse Mg_2Si precipitates, intermetallics and pores measured by 3-D image analysis of SRCT are 0.25%, 0.57% and 0.05%, respectively. More details on the manufacturing process, the microstructure and mechanical properties of the material are described in Ref. [5].

The forging direction, the long transverse direction and the short transverse direction are referenced to the letters L, T and S, respectively. To investigate the damage mechanism via in situ SRCL, 1 mm thick samples taken in a toughness specimen with a thickness of 25 mm (CT25) were used. The loading configuration was T–S, corresponding to the configuration with the minimum toughness value. The first letter represents the loading direction and the second the crack propagation direction. A 5 mm pre-crack was introduced by crack-length controlled fatigue cycling [27]. Electrical discharge machining [28] was used to cut the CT25 specimen into 1 mm thick slices, so that the dimensions of the final specimens for SRCL imaging were $(60 \times 60 \times 1)\ mm^3$.

Two of such specimens from the center of the specimen CT25 were selected: one for the test with a servo-hydraulic machine, the other for investigation via in situ SRCL. The specimens were covered with paint speckles, which serve as markers for the mark-tracking method [29]. The two tests

Table 1
Chemical composition of AA6061 alloy (wt.%).

AA6061	Si (%)	Mg (%)	Fe (%)	Cr (%)	Cu (%)	Mn (%)	Zn (%)	Ti (%)
wt.%	0.65	1.01	0.24	0.18	0.30	0.09	0.20	0.02

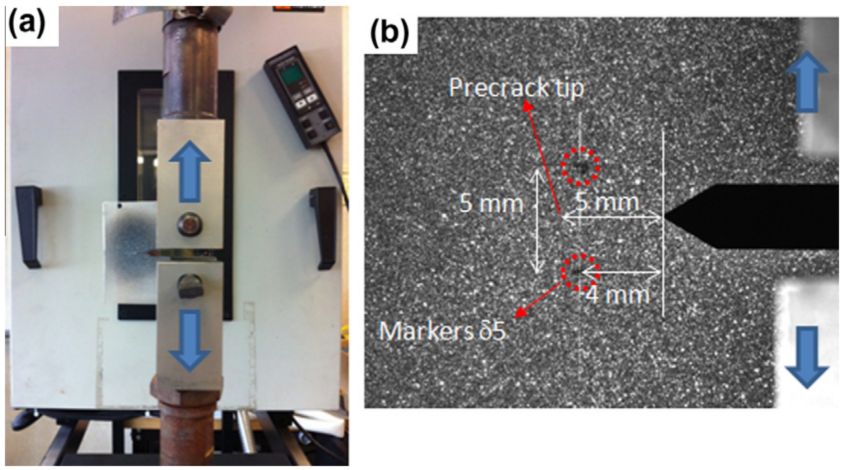

Fig. 1. (a) Configuration of tests with servo-hydraulic machine (anti-buckling device not shown); (b) optical image of the position of markers $\delta5$ compared to the pre-crack tip for the measurement of $\delta5$.

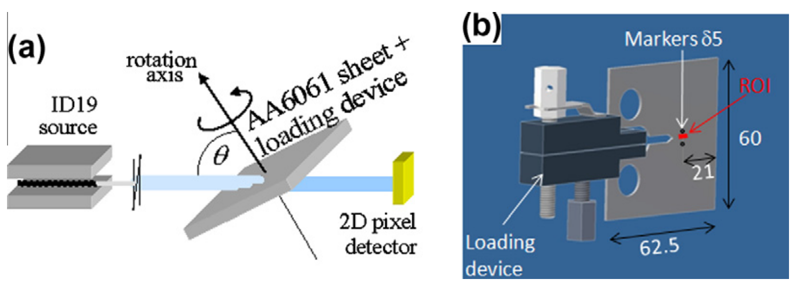

Fig. 2. SRCL test: (a) schematic drawing of SRCL installed at ID19 beamline at the ESRF [33], (b) loading device and the precracked specimen (thickness 1 mm) with $\delta5$ markers and region of interests (ROI) that are scanned.

are complementary since the first one is carried out with a standard loading tests machine but without 3-D image acquisition (Fig. 1a), and the second is performed at the synchrotron facility with a simple loading device that does not measure the force [20] (Fig. 2b).

2.2. Loading tests using a servo-hydraulic machine

In order to measure fracture mechanics parameters during the crack propagation, one specimen was loaded by a servo-hydraulic machine with a loading rate of 8.3 $\mu m\ s^{-1}$. An anti-buckling device was used to prevent the sample from significant buckling and out-of-plane motion [30]. In addition, video monitoring has been used to record the relative displacement of two markers positioned on the surface of specimen separated by 5 mm [30,31] (Fig. 1b) by the mark-tracking method. This displacement is noted $\delta5$ (crack tip opening displacement). We noticed only a small dispersion of the results, and one force–$\delta5$ curve is presented in Fig. 3.

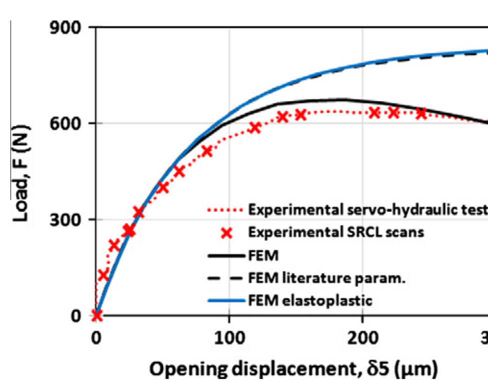

Fig. 3. F–$\delta5$ curve of SRCL test obtained by servo-hydraulic machine with each cross a scan of SRCL and finite-element simulations for different damage parameters.

2.3. In situ SRCL test

The in situ SRCL test was performed on ANKA's laminography set-up [32] installed at beamline ID19 [33] of the

European Synchrotron Radiation Facility (ESRF) in Grenoble, France (Fig. 2a). Details of the experimental method and image reconstruction are given in Refs. [34,35]. We used an axis inclination angle of ~32.5° ($\theta = 57.5°$) and a monochromatic beam of 19 keV X-ray energy. Volumes were reconstructed from angularly equidistant 2000 projections with an exposure time of each projection of 100 ms. A voxel size of 0.7 μm was chosen. To emphasize the difference of gray level among different phases, propagation-based phase-contrast imaging has also been applied [36,37].

The loading was achieved via a two-screw displacement-controlled wedging device, i.e. one that controls the specimen crack mouth opening displacement (CMOD) (Fig. 2b). As for the loading tests with the servo-hydraulic machine, an anti-buckling device was also used. The entire rig was mounted in a dedicated plate that was removed from the SRCL rotation stage between loading steps. The loading was applied via stepwise increases in the $\delta 5$ measured by the mark-tracking method. A scan was carried out between each loading. Knowing that the scatter between specimens is low, the scans of SRCL were plotted on the Force–$\delta 5$ curve obtained by servo-hydraulic tests. The curve is plotted in Fig. 3 with each cross corresponding to a SRCL scan [20]. In total, 15 scans were performed, but only six of them are shown in the qualitative experimental results.

2.4. Method and tools for the post processing

For 3-D damage (voids and crack) representation, a simple gray value threshold was used to segment damage; a Visualization Toolkit (VTK) software routine was used to render the 3-D datasets and produce the 3-D images.

To quantify the damage evolution during crack initiation and propagation, the SRCL 3-D images were analyzed by using the image processing toolbox [38] of the software Matlab. Fig. 4a shows the microstructure of the as-received material with the presence of the pre-crack, the coarse Mg2Si precipitates (dark gray), the intermetallics (white) and the cavities (black) in the aluminum matrix. White phase-contrast fringes can be seen around cavities. In order to eliminate these fringes, a subtraction operation is performed after threshold on all white voxels that are superimposed on dilated cavities.

This quantitative analysis was conducted in a region of interest (ROI) of (140 × 140 × 2100) μm^3 ahead of the pre-crack tip at mid-thickness (Fig. 2b). The long direction of the ROI corresponds to the crack propagation direction (S direction). This region was then cut into zones of 70 μm depth along this direction. Volume fraction values were calculated in these zones (140 × 140 × 70 μm^3 per zone). The ROI size is chosen in accordance with the average distance between void clusters (~150 μm) previously measured by 3-D SRCT on CT specimen performed after interrupted toughness test.

3. Experimental results

3.1. Qualitative observations of ductile fracture

2-D sections taken in the plane TS at mid-thickness of the specimen are shown in Fig. 4a–f corresponding to six

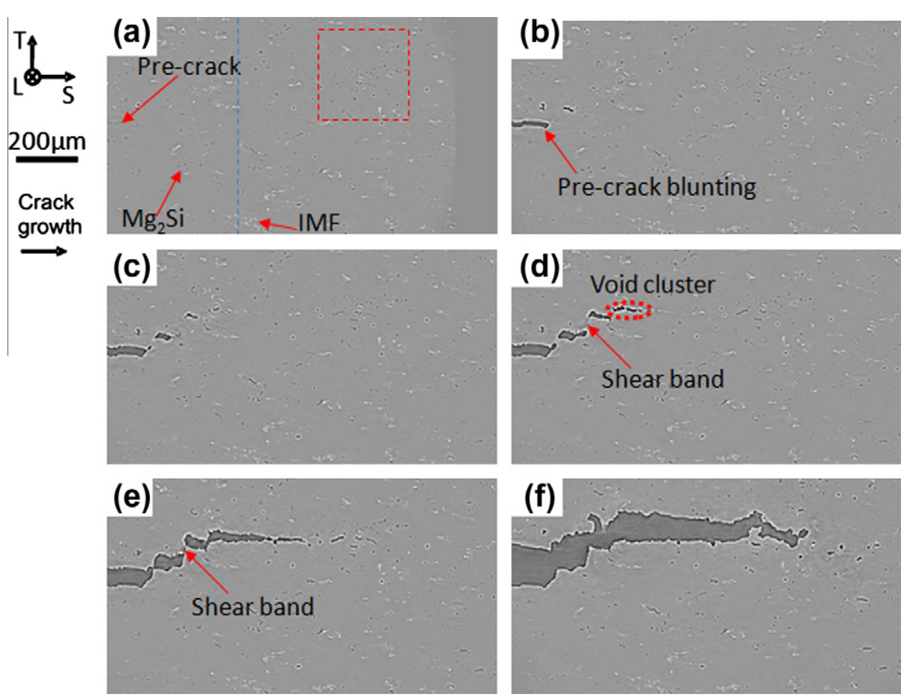

Fig. 4. 2-D sections of SRCL at mid-thickness of specimen at $\delta 5$: (a) initial (=0 μm), (b) $\delta 5 = 23$ μm, (c) $\delta 5 = 50$ μm, (d) $\delta 5 = 62$ μm, (e) $\delta 5 = 83$ μm, (f) $\delta 5 = 153$ μm. Information on the Supplementary loading steps is given in video 1.

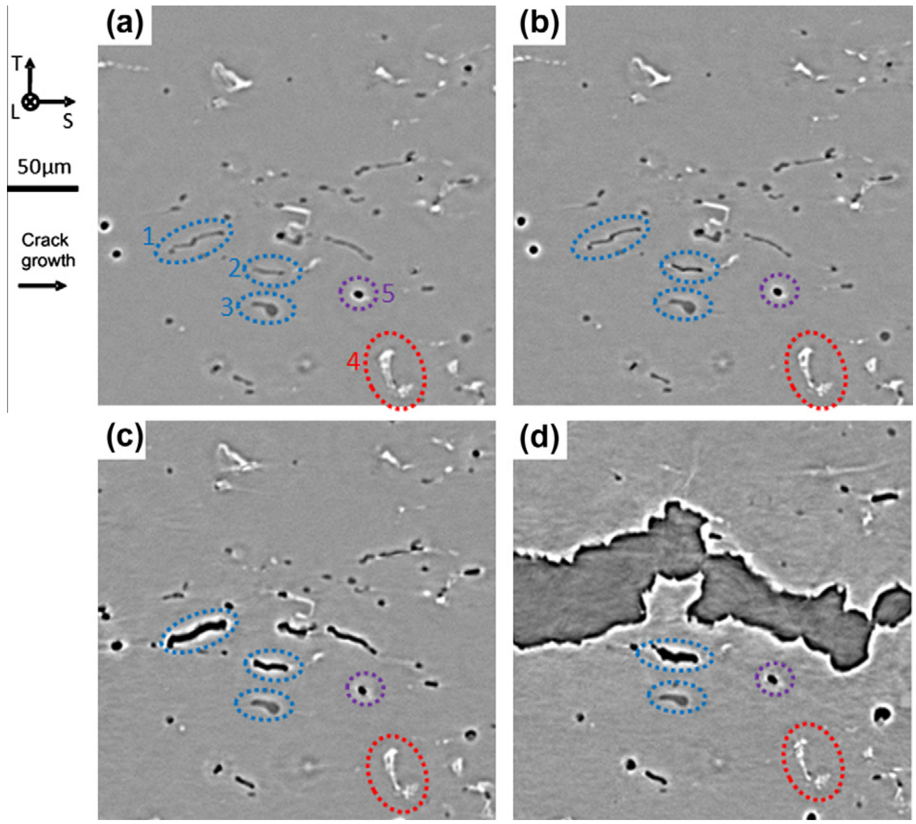

Fig. 5. Zoom of the region circled in red in Fig. 4 with $\delta5$ at: (a) initial, (b) $\delta5 = 23$ μm, (c) $\delta5 = 83$ μm, (d) $\delta5 = 153$ μm. Information on the Supplementary loading steps is given in video 2.

loading steps. The video files associated with this work are given as Supplementary data.

Fig. 4a shows the microstructure of the as-received material. It is observed that coarse Mg_2Si precipitates and intermetallics are elongated and aligned in the L direction. The initial pores have roughly a spherical shape.

Fig. 4b shows sections taken at $\delta5 = 23$ μm with a load of 263 N. A cavity is formed at 40 μm in front of the crack tip and 45° with respect to the loading direction. We also note a pre-existing void present in the material above the crack front. The pre-crack tip blunting can be observed at this stage [39]. Fig. 4c corresponds to $\delta5 = 31$ μm with a load of 323 N; coarse Mg_2Si precipitates at 45° with respect to the loading direction acted as void nucleation sites. The closer the cavity to the crack, the higher the void growth rate.

As observed experimentally [40,41] and also assessed computationally [42], the localization band between voids is controlled by the local distribution of voids, the presence or not of secondary voids, the local stress state and the shape of the voids. Here two clearly distinguishable types of void coalescence can be observed in Fig. 4d at $\delta5 = 62$ μm. In the first type, cavities nucleated from coarse precipitates grow continuously until the voids impinge together. This phenomenon is called void coalescence by internal necking [40]. In the second type, shear bands are forming between cavities initiated from coarse precipitates. These void sheets are oriented at 45° to the loading direction, corresponding to the plastic zone direction ahead of the crack tip. This change of crack propagation path is called crack bifurcation, as shown in Refs. [43,44]. In these localization bands, micro-voids are initiated from a secondary population of smaller precipitates. It can be found in the literature [45–48] that such smaller precipitates refer to dispersoids of chrome and manganese. The stress triaxiality is expected to be at a maximum at the mid-thickness of specimen, and should therefore favor void growth and coalescence by internal necking. This process is then bypassed by the formation of shear bands containing micro-voids before joining the crack.

From Fig. 4e ($\delta5 = 83$ μm, force = 513 N) we see that the crack starts to progress perpendicular to the loading direction. As the grains are elongated along the S direction and coarse precipitates are distributed on grain boundaries [5], the crack propagation is likely to follow an intergranular mode. In Fig. 4c and d, the crack hesitates to propagate from the top or the bottom side of the grain boundary and the intergranular fracture mode is dominant in the crack propagation process.

Fig. 5 shows the zoom of a region on the crack propagation path with a distance of 570 μm ahead of the pre-crack tip (circled in red[1] in Fig. 4a), where we can find coarse Mg_2Si precipitates (objects 1, 2 and 3 circled in blue in

[1] For interpretation of color in Figs. 3–8, the reader is referred to the web version of this article.

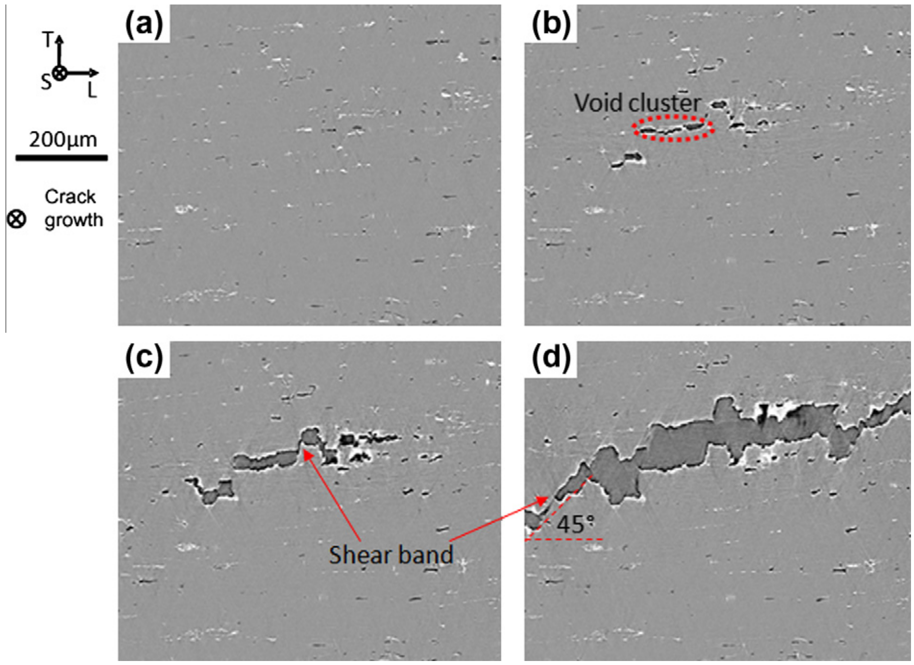

Fig. 6. 2-D sections in the through-thickness plane (through the blue line in Fig. 4a) at 290 μm ahead of the fatigue pre-crack tip with $\delta 5$ at: (a) initial state, (b) $\delta 5 = 62$ μm, (c) $\delta 5 = 83$ μm, (d) $\delta 5 = 153$ μm. Information on the Supplementary loading steps is given in video 3.

Fig. 5a), iron-rich intermetallics (object 4 circled in red in Fig. 5a) and initial pores (object 5 circled in purple in Fig. 5a).

Elongated coarse Mg_2Si precipitates (objects 1 and 2) start to be damaged by precipitate/matrix interface decohesion first from $\delta 5 = 23$ μm (Fig. 5b). This can be seen by the particle that becomes darker and is surrounded by a white edge. This is due to the fact that when the particle fractures a void nucleates and the void particle or void matrix interface leads to strong phase contrast in the used imaging mode [36]. In other words the white surrounding area around the black spot is a hint for the presence of a void and not a particle. Void growth is shown in Fig. 5c, where almost all elongated coarse Mg_2Si precipitates acted as void nucleation sites and their volume increases rapidly in the loading direction, i.e. along the T direction. On the contrary, neither round coarse Mg_2Si (object 3) nor iron-rich intermetallics (object 4) are touched by the damage. Also, no void growth was observed for initial pores (object 5). The crack has then passed through this region (Fig. 5d) and the damaged elongated coarse Mg_2Si precipitates coalesce with the crack.

Fig. 6a–d shows reconstructed 2-D sections of the material in the through-thickness (TL) plane. This plane was chosen with regard to the feature indicated in Fig. 4a through the blue line at 290 μm ahead of the pre-crack tip and is followed for all sections. The micromechanism observed is similar to TS sections (Fig. 4). It is observed that precipitates are elongated and aligned along the L direction, which results in a small distance between them. Void coalescence by internal necking occurs and void clusters are formed. It can be seen from Fig. 6b and c that the crack center does not cover the entire sheet thickness as it forms a triangle where the phenomenon of tunneling occurs, as observed in Refs. [20,25]. In Fig. 6d, the voids on the left of the image, which are oriented and aligned at ~45° with respect to the loading direction, coalesce with the crack via a shear band containing micro-voids. This is the start of the flat-to-slant crack transition [49].

SRCL makes it possible to visualize damage in three dimensions, as shown in Figs. 7 and 8, where damage is segmented and visualized in the TS and LS planes, respectively. In these figures, the crack and voids are shown in a region of $T \times L \times S = (490 \times 840 \times 1400)$ μm^3 around the mid-thickness at different values of $\delta 5$. Figs. 7a and 8a show the as-received material with few homogeneously distributed pre-existing voids. At $\delta 5 = 23$ μm (Figs. 7b and 8b), pre-crack blunting can be seen with voids in front of the crack. Some penny-shaped void clusters (circled in red in Figs. 7 and 8) are aligned and elongated along the S and L directions. These an isotropically distributed penny-shaped void clusters are detrimental for the toughness and may cause toughness anisotropy in this alloy [2,50–52]. As in Fig. 4c–d, we observed the crack bifurcation in Fig. 7c–d. A flat triangularly shaped crack, so-called tunneling, is formed in Fig. 8c and d surrounded in black, as discussed in Ref. [53]. This tunneling phenomenon is observed in situ for the first time in three dimensions during the crack propagation. Different authors have linked this triangle shape to the difference of stress triaxiality between the center and the surfaces of the specimens [54–56]. The surface is in a pure plane stress state involving thus a fracture strain larger than in the center where the stress triaxiality is larger.

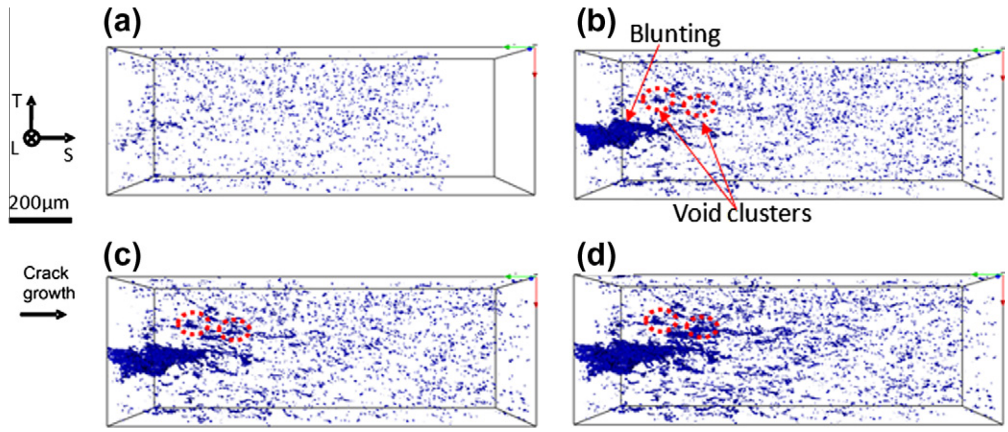

Fig. 7. 3-D volume (T × L × S = 490 × 840 × 1400 µm^3) showing crack and voids in TS plane for $\delta 5$ at: (a) initial, (b) $\delta 5 = 23$ µm, (c) $\delta 5 = 50$ µm, (d) $\delta 5 = 62$ µm.

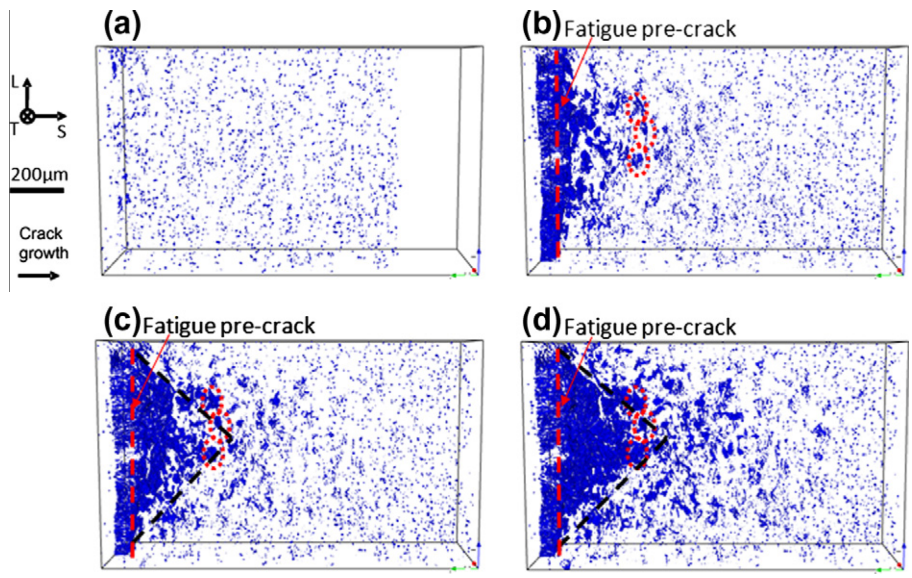

Fig. 8. 3-D volume (T × L × S = 490 × 840 × 1400 µm^3) showing crack and voids in LS plane for $\delta 5$ at: (a) initial, (b) $\delta 5 = 23$ µm, (c) $\delta 5 = 50$ µm, (d) $\delta 5 = 62$ µm.

3.2. Quantitative experimental results

The quantitative damage evolution ahead of the crack is represented as a function of $\delta 5$ and the position of the crack tip along the crack propagation direction in the center of the specimen. As discussed qualitatively in Section 3.1, the damage evolution with the presence of a pre-crack can be divided into two stages: the pre-crack blunting followed by the ductile crack propagation.

Fig. 9a and b represents these two stages. Until $\delta 5 = 31$ µm, the pre-crack opens continuously without propagation (Fig. 9a). This pre-crack blunting is accompanied by the appearance of voids in front of the crack nucleating on Mg_2Si particles. The volume fraction of these voids corresponds to a value of ~1%. From $\delta 5 = 50$ µm onwards (Fig. 9b), the voids coalesce with the crack. The crack propagates step by step in a discontinuous manner. In fact, after each step of propagation, a phase of void growth ahead of the crack tip is seen before they coalesce with the crack. For example, the void volume fraction ahead of the crack at a $\delta 5 = 62$ µm is 0.3%, which is too low to coalesce with the main crack. A new void development stage by nucleation and growth is necessary.

The critical volume fraction for void–crack coalescence can be deduced from Fig. 9. We observe that the coalescence of voids with the crack takes place as soon as the void volume fraction attains a value of ~1% ahead of the crack. It is noted that this critical volume fraction is dependent on the size of the ROI. Here the same order of magnitude as the mean distance between void clusters (~150 µm) is used as ROI dimensions. The result is obtained with a ROI of (140 × 140 × 70) µm^3. It is important to use the same element size in the finite-element simulations with this critical void volume fraction.

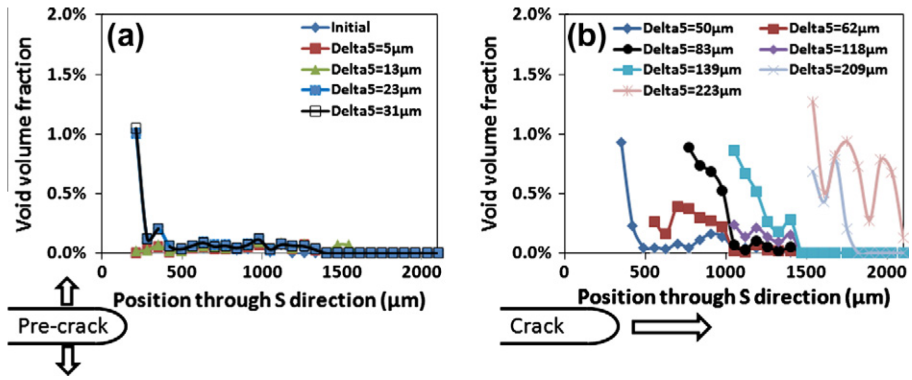

Fig. 9. Evolution of void volume fraction ahead of the crack in function of the position of crack tip through the crack propagation direction at different $\delta5$ in the stage of: (a) pre-crack blunting, and (b) crack propagation.

Beyond the force maximum corresponding to $\delta5 \approx 200$ µm (see Fig. 3), the crack is slanted but similar void volume fractions as for flat crack initiation are found.

4. Modeling

4.1. Parameter identification

The material model is described in Appendix A including the Voce hardening law [57] and the Gurson–Tvergaard–Needleman (GTN) damage model [23,24] where the material damage is associated with a void volume fraction. The main material characteristic parameters included in the models are: (i) parameters of the hardening law; (ii) pre-existing voids and void nucleation parameters; (iii) void growth parameters; and (iv) void coalescence parameters.

The hardening curve is experimentally measured using tensile tests performed on smooth specimens. Beyond uniform elongation of the specimen, the true stress/strain tensile relationship was determined by using the Bridgman correction [58]. The parameters of isotropic Voce hardening law have been fitted to the experimental data, which leads to the values presented in Table 2. The Voce law only describes stage III. The adjustment of the law is in good agreement with the experimental data. Stage IV could be neglected.

As mentioned in Section 3.1, the coarse Mg_2Si precipitates start to be damaged in the very early loading stage. This has been confirmed in in situ SEM tensile tests (not shown here) where the coarse Mg_2Si precipitates fracture already in the elastic part of the stress–strain curve. As a consequence, these precipitates are considered as pre-existing voids f_0 in the simulations.

Cavities nucleating on iron-rich intermetallics are taken into account in the void nucleation parameters. The volume fraction of iron-rich intermetallics obtained by SRCT is considered as the maximum value of the voids that could be nucleated, f_n. The two other parameters of the void nucleation law (ε_{n0} and s_{n0}) are determined by fitting the evolution of density of cavities measured by images analysis during in situ SEM tensile tests and the void nucleation law (not presented here).

Table 2
Parameters identified for SRCL finite element simulations.

(i) Voce hardening law				
E in GPa	υ	σ_0 in MPa	σ_s in MPa	b
70	0.33	288	375	12
(ii) Pre-existing voids and void nucleation				
f_0	f_n	ε_{n0}	s_{n0}	
0.25%	0.57%	10%	0.1	
(iii) Void growth				
q_1	q_2			
1.5	1			
(iv) Void coalescence				
f_c	δ	f_f		
1%	∞	1%		
(v) Element sizes				
$(140 \times 140 \times 140)$ µm^3				

The values proposed by Tvergaard [24] ($q_1 = 1.5$ and $q_2 = 1$) are used as void growth parameters in the GTN model.

The quantitative analysis described in Section 3.2 provides us the critical void volume fraction at which the crack propagates. Crack extension is calculated using the parameter f_f. The crack extends over one element when f has reached this critical value $f_f = 1\%$ throughout the entire element. It is noted that this value is obtained experimentally with a ROI of $(140 \times 140 \times 70)$ µm^3 in front of the crack. The same element size must be used in finite-element analysis, which is $(70 \times 70 \times 70)$ µm^3 with the symmetry condition around the center of the specimen.

For the present material, two reasons lead us to consider that the material loses its strength once the void coalescence begins. First of all, we cannot observe any coalescence between voids without involving the crack, which means that the crack begins to propagate at the same time as or earlier than void coalescence at the present stress state. Secondly, it was observed previously by ex situ SRCT tensile tests that the damage evolution is extremely rapid after the coalescence has started. Therefore the critical void volume fraction at coalescence f_c is assumed to be the same as the critical value at which the crack extends f_f and the acceleration factor $\delta = (f_u - f_c)/(f_f - f_c)$ is thus infinite.

To sum up, the parameters used for the finite-element simulations are resumed in Table 2.

4.2. Model predictions

The finite-element simulation technique is described in Appendix B. The simulation results for SRCL tests with parameters in Table 2 are presented in the following section.

Figs. 3 and 10 show the experimental and simulation results for the SRCL tests. A relatively good fit is achieved for the F–$\delta 5$ curve by using the parameters given in Table 2. The load obtained from the simulation is only slightly above the experimental results (see Fig. 3). The result with typical parameters from the literature [25,59] is also presented for comparison, where a critical void volume fraction at coalescence $f_c = 4.5\%$ and an acceleration factor $\delta = 3$ are used (blue curve in Fig. 3). It is observed that the load from simulation using typical parameters from the literature is overestimated and is little different from the elastoplastic simulation. Our good result of the simulation provides an independent method to identify physically the parameters by a local approach and direct in situ observation. Although the GTN model used in this paper is known to be dependent on mesh size [60–62], neither material model parameters nor element size are identified by parameter fitting in our experimental parameter identification procedure.

The comparison between simulation and experimental results of void volume fraction ahead of the crack tip is shown in Fig. 10 for different $\delta 5$. The coarse Mg_2Si precipitates are considered as voids initially in the simulations, which is not the case in experiments; therefore the void volume fraction value far ahead of the crack is 0.25% (volume fraction of coarse Mg_2Si precipitates) in simulation and 0% for the experiments. At the beginning of crack propagation ($\delta 5 = 50$ μm) and before the unstable stage of crack propagation ($\delta 5 = 139$ μm), the propagation is delayed for

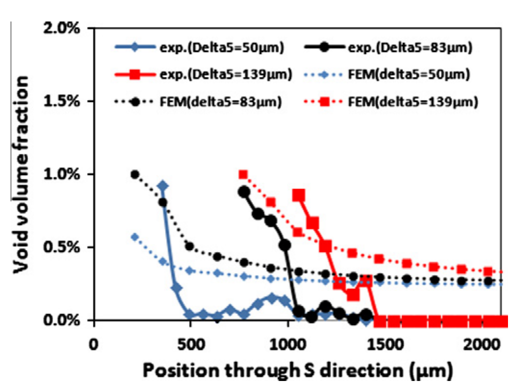

Fig. 10. Experimental and simulation of void volume fraction evolution ahead of the crack in function of the position of crack tip through the crack propagation direction at different $\delta 5$.

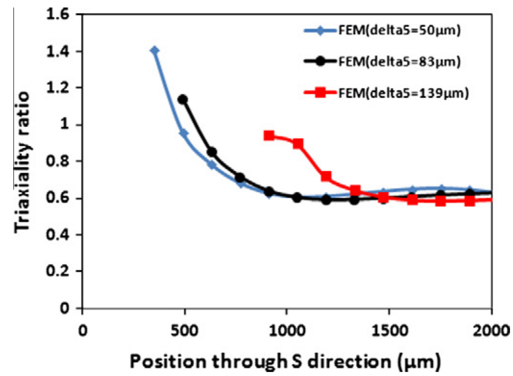

Fig. 11. Stress triaxiality ratio calculated at mid-thickness as a function of the distance to the crack tip.

~250 μm in the simulation and at $\delta 5 = 83$ μm the delay reaches ~500 μm. It is noted that the simulation does not account for void sheeting/shear decohesion that has been observed experimentally. However, via introducing the measured final volume fraction in the model we indirectly account for the fast coalescence stage.

The calculated levels of stress triaxiality at mid-thickness are shown in Fig. 11 as a function of the distance to the pre-crack tip. At pre-crack blunting stage, the level of stress triaxiality attains 1.4 while it decreases to 1 during crack propagation. This change in level of stress triaxiality is also consistent with the change in observed void growth kinetics. While for crack initiation some void growth could be seen, this is much more limited when the crack propagates.

The equivalent strain field at mid-thickness is shown in Fig. 12 at $\delta 5 = 62$ μm. The plastic zone ahead of the crack tip extends over two rows of elements which is consistent with the fact that the crack initiates with a bifurcation during the experiment. However, despite the relatively fine mesh used here the plastic zone shape is not resolved finely enough to link the observed crack shape with the plastic zone shape (Section 3.1).

5. Discussion

In the present study, an in situ synchrotron radiation computed laminography (SRCL) test was used to analyze the crack initiation and propagation in bulk material. We clearly identified the predominant detrimental role played by the coarse Mg_2Si precipitates in the damage process contrary to studies showing a preponderant role of the iron-rich intermetallics [6,8–10].

Quantitative SRCL analysis is for the first time conducted in this study and is used to identify parameters of the GTN damage model. The final void volume fraction at failure f_f is calibrated for the first time based on 3-D microstructural measurement in a ROI corresponding to the FE element size based on mean distance between void clusters. It would be interesting to know if the same result can be found with different ROI/element size. In an initial attempt using larger and smaller ROI/element size (factor 0.5 and 2) for this analysis we have encountered

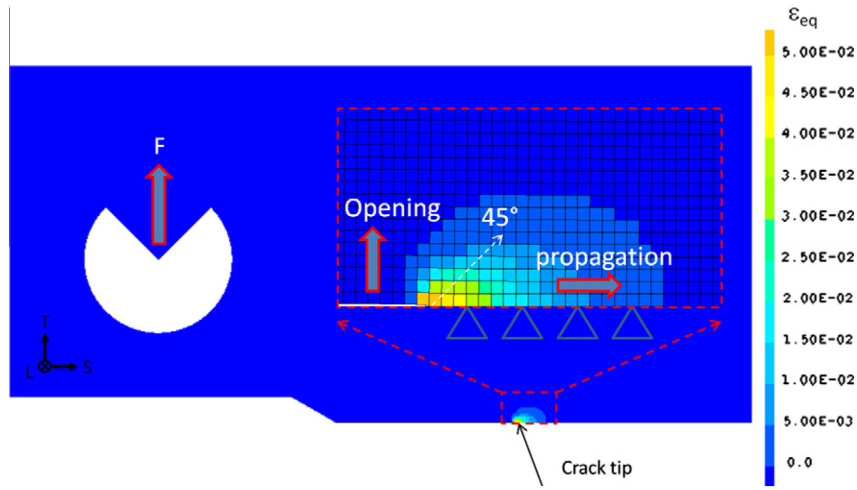

Fig. 12. Equivalent strain at mid-thickness of specimen obtained by finite-element simulation at $\delta 5 = 62$ μm.

convergence problems. With the in situ 3-D parameter identification procedure based on SRCL measurement, the crack initiation and propagation is correctly simulated. In order to test the robustness of this original method, the same procedure needs to be validated on other materials with various metallurgical features.

It is observed in three dimensions by SRCL that two types of coalescence co-exist in the crack propagation process: internal necking and void sheeting or even intergranular ductile fracture. These features are not clearly considered in the GTN model but are hidden in the critical coalescence and failure parameters (f_c and f_f). The typical parameters used in the literature are much higher than our calibration conducted by 3-D SRCL measurement ($f_c = 4.5\%$, $f_f = 25.2\%$ in the literature vs. $f_c = f_f = 1\%$ in SRCL measurement). It seems that parameters in the literature are too optimistic and neglect coalescence mechanisms other than internal necking. Here we capture these mechanisms indirectly via measurement of the parameter f_f.

6. Conclusions

A pre-cracked laterally extended 1 mm thick AA6061-T6 alloy sheet was used in the in situ synchrotron radiation computed laminography (SRCL) experiments, which provide not only qualitative in situ observation of fracture mechanisms in crack initiation and propagation but also quantitative measurement of void growth ahead of the crack tip with which material models are identified and validated.

At the early stage of loading, pre-crack blunting has been observed in three dimensions accompanied by the formation of voids at 45° in front of the pre-crack. Two types of coarse precipitates are present in the alloy: coarse Mg_2Si precipitates and iron-rich intermetallics. Roles played by these precipitates in the fracture mechanism have been clearly distinguished here: coarse Mg_2Si precipitates play a preponderant role as they are damaged at the early loading stage in contrast to iron-rich intermetallics, which break much later. As these two coarse precipitates are intergranularly distributed, aligned and elongated through the crack propagation direction, the intergranular mode of crack propagation is thought to be dominant.

The crack propagation takes place by two classes of void coalescence. The neighboring voids initiated from coarse precipitates coalesce by internal necking and become penny-shaped void clusters, which are then linked with the crack by shear bands containing micro-voids, nucleated possibly at dispersoids. The tunneling phenomenon has been observed in three dimensions during the flat crack propagation.

The quantitative void volume fraction analysis has been conducted in front of the crack tip. A discontinuous crack propagation regime was highlighted. The crack propagates by a repetitive process of void nucleation–growth–coalescence ahead of the crack tip. As soon as a critical void volume fraction ahead of the crack is attained, the crack links with these voids and propagates for a certain length. This critical value was evaluated at 1% for a region of interest of $(140 \times 140 \times 70)$ μm^3, which was used as the critical void volume fraction for the failure of elements with the same element size in a Gurson–Tvergaard–Needleman (GTN) micromechanical damage model.

Parameters of the GTN model have been identified by using quantitative results of SRCL and SRCT. In this identification procedure, all parameters were identified experimentally by a local approach and in situ observation without parameter adjustment. Finite-element simulation conducted on the SRCL specimen shows the good predictive capabilities of the model.

Acknowledgements

The authors would like to thank Pierre Wident and David Leboulch from CEA as well as Henry Proudhon, Frank Nguyen and Julie Heurtel from Centre des Materiaux of Mines ParisTech for technical supports.

Appendix A. Material models

A.1. Voce hardening law

The plastic hardening is represented by a Voce-type stress saturation equation and is expressed as follows [57]:

$$\sigma = \sigma_s(\sigma_0 - \sigma_s)\exp(-b\varepsilon)$$

where σ_0 is yielding stress and σ_s and b are undamaged material constants.

A.2. GTN damage model

The Gurson–Tvergaard–Needleman (GTN) micromechanical model [23,24] is used to introduce damage and is represented by a single scalar variable, the void volume fraction f. The plastic flow potential Φ is written:

$$\Phi = \frac{\sigma_{eq}^2}{\sigma_y^2} + 2q_1 f^* \cos h\left(\frac{3q_2}{2}\frac{\sigma_m}{\sigma_y}\right) - 1 - (q_1 f^*)^2 = 0$$

The function f^* is the effective porosity and is justified to describe the onset of the void coalescence beyond a critical porosity f_c. The void coalescence is represented by an acceleration of damage rate [24], with:

$$f^* = \begin{cases} f, & f < f_c \\ f_c + \delta(f - f_c), & f \geq f_c \end{cases}$$

where q_1, q_2 are void growth parameters involving the yield surface, σ_y is the yielding stress of non-damaged material, $\delta = \frac{f_u - f_c}{f_f - f_c}$ is the void coalescence acceleration factor. The material loses its stress carrying capacity at $f = f_f$. In this case the crack is assumed to propagate.

The evolution of void volume fraction includes two parts, the growth of the existing voids and the nucleation of new voids. The increase of void volume fraction in the model is written as:

$$\dot{f} = \dot{f}_g + \dot{f}_n$$

Because the matrix material is incompressible, the growth part $\dot{f}_g$ is related to the equivalent plastic strain $\dot{\varepsilon}_{eq}^p$ and is described as:

$$\dot{f}_g = (1 - f)\dot{\varepsilon}_{eq}^p$$

Chu and Needleman [63] expressed the void nucleation rate by a distribution function considering the heterogeneous nucleation process. This void nucleation law is dependent exclusively on the equivalent plastic strain:

$$\dot{f}_n = A\dot{\varepsilon}_{eq}^p$$

The coefficient A is selected so that the void nucleation follows a normal distribution function [63] described as:

$$A = \frac{f_{n0}}{s_{n0}\sqrt{2\pi}}\exp\left(-\frac{1}{2}\left(\frac{\varepsilon_{eq}^p - \varepsilon_{n0}}{s_{n0}}\right)^2\right)$$

where f_{n0} is the maximum value of nucleated void fraction, ε_{n0} is the mean strain for which the nucleation appears and s_{n0} represents the deviation of the mean strain for which the nucleation appears.

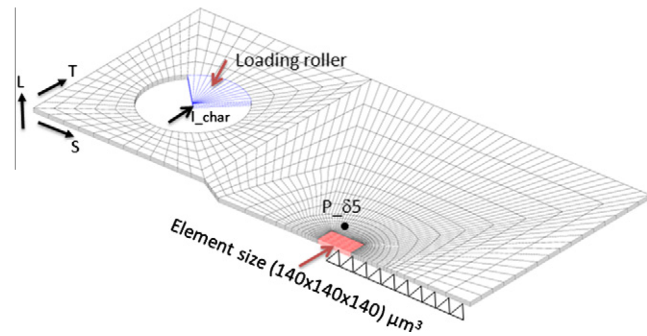

Fig. 13. 3-D mesh of the quarter of the SRCL specimen with loading roller.

Appendix B. Simulation technique

The GTN model was implemented in the finite-element software Cast3m (http://www-cast3m.cea.fr/), developed by the CEA in France. Due to symmetry, a quarter of the three-dimensional SRCL specimen is meshed by using quadratic elements with reduced integration (Fig. 13).

When modeling crack propagation using continuum damage mechanics, the crack is a thin volume with a height which is half the element height in the case of quadratic elements with reduced integration (type CU20 with 20 nodes and eight Gauss points) [62]. The mesh is refined in the crack region with element size of ~(140 × 140 × 140) μm^3, which means (70 × 70 × 70) μm^3 for inter-Gauss point size equivalent to the size of ROI in the quantitative experimental analysis in Section 3.2 with respect to the symmetric condition. The loading roller of experimental setup is modeled as a rigid body. The friction is neglected between roller and specimen. Loading is applied via imposed displacement through the Y-axis at line l_char. As in the experimental analysis, the $\delta 5$ is calculated at every loading step as twice the displacement of the marker P_δ5 positioned on the surface of specimen at 2.5 mm through the Y-axis.

Appendix C. Supplementary data

Supplementary data associated with this article can be found, in the online version, at http://dx.doi.org/10.1016/j.actamat.2013.01.035.

References

[1] Garrison Jr WM, Moody NR. J Phys Chem Solids 1987;48:1035.
[2] Pardoen T, Hutchinson JW. Acta Mater 2003;51:133.
[3] Alwitt RS. The aluminium-water system. New York: Dekker; 1976.
[4] Gang L, Jun S, Ce-Wen N, Kang-Hua C. Acta Mater 2005;53:3459.
[5] Shen Y, Garnier J, Allais L, Crepin J, Ancelet O, Hiver JM. Proc Eng 2011;10:3429.
[6] Agarwal H, Gokhale AM, Graham S, Horstemeyer MF. Mater Sci Eng A-Struct Mater Prop Microstruct Process 2003;341:35.
[7] Blind JA, Martin JW. Mater Sci Eng 1983;57:49.

[8] Lugo M, Jordon JB, Horstemeyer MF, Tschopp MA, Harris J, Gokhale AM. Mater Sci Eng A-Struct Mater Prop Microstruct Process 2011;528:6708.
[9] Horstemeyer MF, Gokhale AM. Int J Solids Struct 1999;36:5029.
[10] Agarwal H, Gokhale AM, Horstemeyer MF, Graham S. Aluminum automotive and joining symposia; 2001. p. 43.
[11] Lautridou JC, Pineau A. Eng Fract Mech 1981;15:55.
[12] Pardoen T, Marchal Y, Delannay F. Journal of the Mechanics and Physics of Solids 1999;47:2093.
[13] Shuji T, Keisuke T. Eng Fract Mech 1979;11:231.
[14] Maire E, Zhou S, Adrien J, Dimichiel M. Eng Fract Mech 2011;78:2679.
[15] Gammage JJ, Wilkinson DS. Philos Mag 2005;85:3191.
[16] Toda H, Maire E, Yamauchi S, Tsuruta H, Hiramatsu T, Kobayashi M. Acta Mater 2011;59:1995.
[17] Helfen L, Baumbach T, Mikulik P, Kiel D, Pernot P, Cloetens P, et al. Appl Phys Lett 2005:86.
[18] Moffat AJ, Wright P, Helfen L, Baumbach T, Johnson G, Spearing SM, et al. Scripta Materialia 2010;62:97.
[19] Xu F, Helfen L, Moffat AJ, Johnson G, Sinclair I, Baumbach T. J Synchr Rad 2010;17:222.
[20] Morgeneyer TF, Helfen L, Sinclair I, Proudhon H, Xu F, Baumbach T. Scripta Materialia 2011;65:1010.
[21] Morgeneyer TF, Helfen L, Mubarak H, Hild F. 3D Digital volume correlation of synchrotron radiation laminography images of ductile crack initiation: An Initial Feasibility Study. Exp Mech 2012:1.
[22] Rice JR, Tracey DM. J Mech Phys Solids 1969;17:201.
[23] Gurson AL. Plastic flow and fracture behavior of ductile materials incorporating void nucleation, growth and interaction. Thesis: Brown University; 1975.
[24] Tvergaard V, Needleman A. Acta Metallurgica 1984;32:157.
[25] Morgeneyer TF, Besson J, Proudhon H, Starink MJ, Sinclair I. Acta Mater 2009;57:3902.
[26] Steglich D, Brocks W, Heerens J, Pardoen T. Eng Frac Mech 2008;75:3692.
[27] Brown WF. Review of developments in plane strain fracture toughness testing (ASTM special technical publication 463). Washington, DC: NASA; 1970.
[28] Ho KH, Newman ST. Int J Mach Tools Manuf 2003;43:1287.
[29] Chean V, Robin E, El Abdi R, Sangleboeuf JC, Houizot P. Optics Laser Technol 2011;43:1172.
[30] Schwalbe KH, Newman JC, Shannon JL. Eng Fract Mech 2005;72:557.
[31] Zerbst U, Heinimann M, Donne CD, Steglich D. Eng Fract Mech 2009;76:5.
[32] Helfen L, Altapova V, Hänschke D, Homs-Puron A, Valade JP, Schneider M, et al. Rev Sci Instrum, submitted for publication.
[33] Weitkamp T, Tafforeau P, Boller E, Cloetens P, Valade JP, Bernard P, et al., editors. Sri 2009: The 10th international conference on synchrotron radiation instrumentation, vol. 1234. Melville: American Institute of Physics; 2010. p. 83.
[34] Myagotin A, Voropaev A, Helfen L, Hänschke D, Baumbach T. J Parallel Distrib Comput, submitted for publication.
[35] Helfen L, Myagotin A, Mikulik P, Pernot P, Voropaev A, Elyyan M, et al. Rev Sci Instrum 2011;82.
[36] Cloetens P, Pateyron-Salomé M, Buffière JY, Peix G, Baruchel J, Peyrin F, et al. J Appl Phys 1997;81:5878.
[37] Helfen L, Baumbach T, Cloetens P, Baruchel J. Appl Phys Lett 2009:94.
[38] Toolbox IP. Natck. MA: The MathWorks Inc.; 2011.
[39] Beremin FM. Metall Trans A, Phys Metall Mater Sci 1981;12A:723.
[40] Weck A, Wilkinson DS. Acta Mater 2008;56:1774.
[41] Weck A, Wilkinson DS, Maire E, Toda H. Acta Mater 2008;56:2919.
[42] Tekoglu C, Leblond JB, Pardoen T. J Mech Phys Solids 2012;60:1363.
[43] Rudnicki JW, Rice JR. J Mech Phys Solids 1975;23:371.
[44] Leblond JB, Perrin G, Devaux JC. Bifurcation effects in ductile metals with nonlocal damage. New York: American Society of Mechanical Engineers; 1994.
[45] Jeniski Jr RA. Mater Sci Eng: A 1997;237:52.
[46] Walsh JA, Jata KV, Starke Jr EA. Acta Metallurgica 1989;37:2861.
[47] Van Stone R, Psioda J. Metall Mater Trans A 1975;6:668.
[48] Prince KC, Martin JW. Acta Metallurgica 1979;27:1401.
[49] Morgeneyer TF, Besson J. Scripta Mater 2011;65:1002.
[50] Benzerga AA, Besson J, Pineau A. Acta Mater 2004;52:4623.
[51] Benzerga AA, Besson J, Pineau A. Acta Mater 2004;52:4639.
[52] Lassance D, Fabrègue D, Delannay F, Pardoen T. Prog Mater Sci 2007;52:62.
[53] Bron F, Besson J, Pineau A. Mater Sci Eng: A 2004;380:356.
[54] Lan W, Deng X, Sutton MA. Eng Fract Mech 2010;77:2800.
[55] Zuo J, Deng X, Sutton MA, Cheng C-S. J Press Vessel Technol 2008;130:031401.
[56] James MA, Newman JC. The effect of crack tunneling on crack growth: experiments and CTOA analyses. Kidlington: Elsevier; 2003.
[57] Voce E. J I Met 1948;74:537.
[58] Bridgman PW. Studies in large plastic flow and fracture with special emphasis on the effects of hydrostatic pressure. New York: McGraw-Hill'; 1952.
[59] Steglich D, Wafai H, Besson J. Eng Fract Mech 2010;77:3501.
[60] Rivalin F, Besson J, Pineau A, Di Fant M. Eng Fract Mech 2000;68:347.
[61] Xia L, Shih CF, Hutchinson JW. J Mech Phys Solids 1995;43:389.
[62] Bron F, Besson J. Eng Fract Mech 2006;73:1531.
[63] Chu C, Needleman A. J Eng Mater Technol-Trans ASME 1980;102:249.